

# Metasurfaces with high- $Q$ bound states enabled by eliminating the first Fourier harmonic component in the lattice parameters

Sun-Goo Lee,\* Seong-Han Kim, and Chul-Sik Kee†

*Integrated Optics Laboratory, Advanced Photonics Research Institute,  
Gwangju Institute of Science and Technology, Gwangju 61005, South Korea*

(Dated: December 22, 2024)

Conventional photonic lattices, including metamaterials and photonic crystals, exhibit various interesting physical properties due to the periodic modulations in lattice parameters. Here, we introduce new types of photonic lattices, namely Fourier-component-engineered metasurfaces, that do not possess the first Fourier harmonic component in the lattice parameters, and demonstrate that the metasurfaces support the continuous high- $Q$  bound states near the second stop bands. The concept of engineering Fourier harmonic components in periodic modulations provides a new method to manipulate electromagnetic waves in artificial periodic structures.

Subwavelength photonic lattices with thin-film geometries, such as metasurfaces [1–3] and photonic crystal slabs [4, 5], have attracted significant attention in recent years owing to their substantial abilities of manipulating electromagnetic waves. Unlike the usual thin homogeneous dielectric layers that are governed by the Fresnel equations and Snell’s law [6], photonic lattices can capture the incident light resonantly through the lateral Bloch modes and reemit the light with predesigned electromagnetic responses [7]. By appropriately designing the individual constituents in the lattices, several interesting physical effects and useful applications, which cannot be achieved with conventional dielectric materials, can be realized in an extremely compact format even as a single-layer film [8–10].

Recently, the bound states in the continuum (BICs) with exceptionally high radiative  $Q$  factors in one-dimensional (1D) and 2D planar photonic lattices have been studied extensively. In principle, the BICs with infinite  $Q$  factors can be found as unusual electromagnetic eigenstates that remain well localized in open photonic systems even though they can coexist with the continuous spectrum of outgoing waves [11–14]. The BICs are associated with various fascinating physical phenomena such as the sharp Fano resonances [15], enhanced nonlinear effects [16], and topological nature [17, 18]. Different types of BICs have been studied in versatile planar photonic lattices [19–23]. However, the high- $Q$  BICs introduced in the literatures thus far are strongly sensitive to the wavevector of Bloch modes in the lattices. Hence, the sharp Fano resonances and enhanced nonlinear effects due to the high- $Q$  Bloch modes can be obtained at a discrete specific incident angle. Small variations in the incident angle significantly reduce the resonance  $Q$  factor in the spectral responses.

In this Letter, we introduce the concept of Fourier-component-engineered (FCE) metasurfaces, that do not possess the first Fourier harmonic component in the periodically modulated lattice parameters, and demonstrate that the metasurfaces can support the continuum of high- $Q$  bound states in a wide range of wavevectors instead

of a specific discrete wavevector. Guided modes in 1D or 2D FCE metasurfaces exhibit noticeably increased radiative  $Q$  factors because the out-of-plane radiation is due to the first Fourier harmonic component of periodic modulations. Two types of FCE metasurfaces that utilize the spatially engineered dielectric function and thickness profile, respectively, are presented and analyzed.

Figure 1(a) illustrates the simplest representative 1D photonic lattice, i.e., binary diffraction grating (BDG), consisting of high ( $\epsilon_a$ ) and low ( $\epsilon_b$ ) dielectric constant materials. Thickness of the grating is  $d$  and width of high dielectric constant part is  $\rho\Lambda$ , where  $\Lambda$  is the period of the grating. The BDG layer acts as a waveguide as well as a diffracting element because its average dielectric constant  $\epsilon_{avg} = \rho\epsilon_a + (1 - \rho)\epsilon_b$  is larger than that of surrounding medium ( $\epsilon_s$ ). The periodic modulations in the dielectric constant generates photonic band gaps at the Bragg condition  $k_z = qK/2$ , as shown in Fig. 1(b), where  $k_z$  is the Bloch wavevector,  $K = 2\pi/\Lambda$  is the magnitude of the grating vector, and  $q$  is an integer representing the Bragg order. The first stop band ( $n = 1$ ) in the yellow region is not associated with the leaky-wave effects because it is protected by the total internal reflection. Near the second stop band ( $n = 2$ ) in the white region, the leaky-wave effects occur because the Bloch modes are described by complex eigenfrequencies  $\Omega = \Omega_{Re} + i\Omega_{Im}$ . With the time dependence of electric field as  $\exp(-i\Omega t)$ , the imaginary part  $\Omega_{Im}$  represents the radiative loss. In this study, we focus on the second band gap of the fundamental  $TE_0$  mode because high- $Q$  BICs are associated with the second stop bands in many cases. As conceptually illustrated in Fig. 1(c), the second leaky stop band is formed primarily by the direct coupling  $h_2$  with  $|\Delta k_z| = 2K$  between two counterpropagating waves  $\sim \exp(\pm iKz)$ , and secondarily by the radiative coupling  $h_1$  with  $|\Delta k_z| = K$  between the guided and radiating waves [24].

We first show that the coupling processes  $h_1$  and  $h_2$  illustrated in Fig. 1(c) are associated with the first and second Fourier harmonic components, respectively, and the out-of-plane radiation loss is caused by the first Fourier

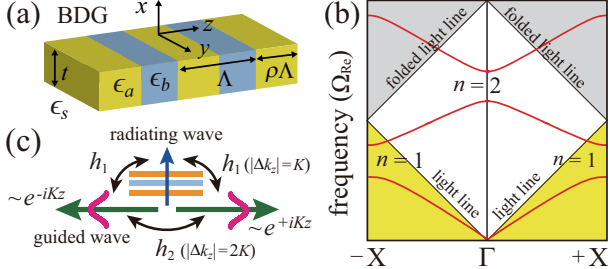


FIG. 1. (a) Schematic of a conventional 1D BDG. (b) With the periodic modulation in the dielectric constant, photonic band gaps open at the Bragg condition  $k_z = qK/2$ . (c) Conceptual illustration of the coupling processes induce the second leaky band gap.

harmonic component. Eigenfrequencies of Bloch modes in the BDGs can be obtained by solving the 1D wave equation given by [25]:

$$\left( \frac{\partial^2}{\partial x^2} + \frac{\partial^2}{\partial z^2} \right) E_y(x, z) + \epsilon(x, z) k_0^2 E_y(x, z) = 0, \quad (1)$$

where  $k_0$  denotes the wave number in free space. Equation (1) can be solved by expanding the periodic dielectric function  $\epsilon(x, z)$  in a Fourier series and the electric field  $E_y$  as a Bloch form [26]. For the BDG with the inversion symmetry, the dielectric function can be expanded in an even cosine function series  $\epsilon(z) = \sum_0^\infty \epsilon_n \cos(nKz)$  where the Fourier coefficients are given by  $\epsilon_0 = \epsilon_{\text{avg}}$  and  $\epsilon_{n \geq 1} = (2\Delta\epsilon/n\pi) \sin(n\pi\rho)$ . For clear insight into the formation of the second stop band, we use a simple semianalytical approach in which only the zeroth, first, and second Fourier harmonics are retained for the dielectric function and the spatial electric field distribution is approximated as  $E_y(x, z) = [A \exp(+iKz) + B \exp(-iKz)] \varphi(x) + E_{\text{rad}}$ , where  $A$  and  $B$  are slowly varying envelopes of the two counterpropagating waves,  $\varphi(x)$  characterizes the mode profile of the unmodulated waveguide, and  $E_{\text{rad}}$  represents the radiating diffracted wave [27]. Solving the wave equation with the approximated dielectric function and field distributions, the dispersion relations near the second stop band can be written as

$$\Omega(k_z) = \Omega_0 - \left( i h_1 \pm \sqrt{k_z^2 + (h_2 + i h_1)^2} \right) / (K h_0), \quad (2)$$

where  $\Omega_0$  is the Bragg frequency under vanishing index modulation ( $\Delta\epsilon = 0$ ), and the coupling coefficients are given by

$$h_0 = \Omega \int_{-\infty}^{\infty} \epsilon_0(x) \varphi(x) \varphi^*(x) dx, \quad (3)$$

$$h_1 = i \frac{K^3 \Omega^4 \epsilon_1^2}{8} \int_{-t}^0 \int_{-t}^0 G(x, x') \varphi(x') \varphi^*(x) dx' dx, \quad (4)$$

$$h_2 = \frac{K \Omega^2 \epsilon_2}{4} \int_{-t}^0 \varphi(x) \varphi^*(x) dx, \quad (5)$$

where  $G(x, x')$  denotes the Green's function for the diffracted field [24, 28, 29]. Dispersion relations in Eq. (2) can be obtained by calculating the coupling coefficients in Eqs. (3)–(5). Details of the mathematical process to obtain Eq. (2) is provided in Supplemental Material [30].

Equation (2) indicates that the leaky stop band with two band edges  $\Omega^a = \Omega_0 + h_2/(K h_0)$  and  $\Omega^s = \Omega_0 - (h_2 + i 2h_1)/(K h_0)$  opens at  $k_z = 0$ . For the BDG with the inversion symmetry, the coupling coefficient  $h_1$  is generally a complex value, whereas  $h_0$  and  $h_2$  are real values irrespective of lattice parameters. Hence, at the band edge with frequency  $\Omega^a$ , which is obtained when the electric field distribution is an asymmetric (sine) function ( $A = -B$ ), there is no radiation loss because  $\Omega^a$  is purely real. At the  $\Omega^s$  band edge obtained when the field distribution is a symmetric (cosine) function ( $A = B$ ), the radiative loss is maximal with  $\text{Im}(\Omega^s) = -2\text{Re}(h_1)/(K h_0)$ . Except the symmetry-protected BIC with  $\Omega^a$ , Bloch modes near the second stop band generally suffer radiation loss because they have complex frequencies as indicated in Eq. (2). Since the second stop band opens at the second-order  $\Gamma$  point ( $k_z = K$  in the extended Brillouin zone) with the Bragg condition  $k_z = q(\pi/p)$ , where  $p$  is the period of the dielectric constant modulation and  $q$  represents the Bragg order, it is reasonable to interpret that the coupling coefficients  $h_1$  and  $h_2$  represent the second-order Bragg effect due to the first Fourier harmonic,  $\epsilon_1 \cos(Kz)$ , and the first-order Bragg effect due to the second Fourier harmonic,  $\epsilon_2 \cos(2Kz)$ , respectively. Hence, Eq. (2) indicates that near the second stop band, leakage loss of the guided Bloch modes originate from the diffraction effect due to the first Fourier harmonic component. Without  $h_1$ , in the vicinity of the  $\Gamma$  point, guided modes become the BICs irrespective of  $k_z$  with the real eigenfrequencies given by  $\Omega(k_z) = \Omega_0 \pm \sqrt{k_z^2 + h_2^2}/(K h_0)$ . Inspired by the analytical dispersion relations, we introduce and analyze FCE metasurfaces without the first Fourier harmonic component through the rigorous finite element method (FEM) simulations.

In Fig. 2, we compare the key properties of the conventional BDG and those of the corresponding FCE metasurface. As shown in Fig. 2(a), the FCE metasurface has complex dielectric functions  $\epsilon_a - \epsilon_1 \cos(Kz)$  and  $\epsilon_b - \epsilon_1 \cos(Kz)$  when  $|z| < \rho\Lambda/2$  and  $|z| \geq \rho\Lambda/2$ , respectively, while the conventional BDG has simple step-like dielectric functions with  $\epsilon_a$  and  $\epsilon_b$ . Simulated dispersion relations illustrated in Fig. 2(b) show that the second band gap opens at  $k_z = 0$  for both the BDG and FCE metasurface. Dispersion curves for the BDG and FCE metasurface seem similar, and the spatial electric field ( $E_y$ ) distributions in the insets show that symmetry-protected BICs with the asymmetric field distributions appear at the upper band edges in both the BDG and FCE metasurface. However, the noticeable difference between the BDG and FCE metasurface can be seen from the symmetric spatial electric field distributions of the

lower edge mode. While the lower edge mode in the BDG is radiative out of the lattice, that in the FCE metasurface is appropriately localized in the lattice even though it is not protected by the symmetry mismatch. The effect of the first Fourier harmonic component can also be seen clearly by investigating the radiative  $Q$  factors as a function of  $k_z$  plotted in Fig. 2(c). In the conventional BDG, the BIC in the upper band exhibits a  $Q$  factor that is larger than  $10^{15}$  at the  $\Gamma$  point but the  $Q$  values decrease abruptly and approach to the value of  $Q$  factor of leaky modes ( $\sim 10^3$ ) in the lower band as  $k_z$  moves away from the  $\Gamma$  point. Similarly, in the FCE metasurface, the BIC also exhibits a  $Q$  factor that is larger than  $10^{15}$  and the  $Q$  values decrease as  $k_z$  moves away from the  $\Gamma$  point. However, the Bloch modes in both the upper and lower band branches have high  $Q$  values ( $\sim 10^8$ ) in the computational range of  $|k_z| \leq 0.12 K$ . The  $Q$  factors in the FCE metasurface are approximately  $10^5$  times larger than those in the conventional BDG with the same lattice parameters except the profile of the dielectric function.

The symmetry-protected BICs at the  $\Gamma$  point are perfectly embedded eigenvalues with an infinite  $Q$  factor and vanishing resonance line width because they are perfectly decoupled from external waves. In diverse practical applications, quasi-BICs with finite high- $Q$  values and narrow spectral responses via resonant coupling with external waves are favorable. Figure 2(d) illustrates the transmission spectra through the BDG and FCE metasurface for three different values of incident angles  $\theta = 0^\circ$ ,  $1^\circ$ , and  $7^\circ$ . At normal incidence with  $\theta = 0^\circ$ , the BDG structure exhibits only the low- $Q$  resonance by the lower band edge mode. The embedded BIC in the upper band edge mode, a green solid circle in the transmittance curve, do not generate the resonance effect. When  $\theta = 1^\circ$ , simulated transmittance curve through the conventional BDG shows the low- $Q$  resonance by the lower band mode and the high- $Q$  resonance by the upper band mode, simultaneously. As  $\theta$  increases further, the resonance line width by the upper band mode in the BDG increases rapidly and becomes close to that by the lower band mode. Two low- $Q$  resonances by the upper and lower band modes are observed in the spectral response when  $\theta = 7^\circ$ . Similarly, the transmittance curve through the FCE metasurface does not show the embedded BIC in the upper band when  $\theta = 0^\circ$ . However, the resonance line width by the lower band mode in the metasurface is extremely narrow irrespective of the incident angle  $\theta$ , unlike the case of conventional BDG. As  $\theta > 0$  increases, two quasi-BICs by the lower and upper band modes are observed in the transmission curves and the resonance line widths remain narrow when  $\theta = 7^\circ$ . Many efforts have been devoted to realize high- $Q$  resonant modes in photonic crystal structures. However, high- $Q$  modes reported in previous literatures were obtained at specific discrete wavevectors [31]. Because the proposed FCE metasurface can support the continuous quasi-BICs in the vicinity of the second stop

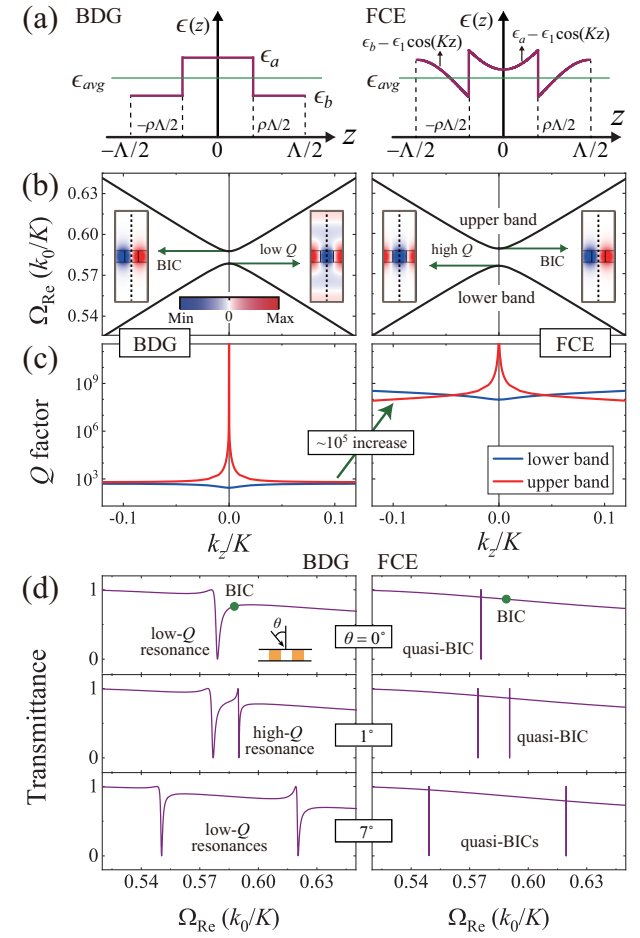


FIG. 2. Comparison between the conventional BDG and FCE metasurface. (a) Dielectric functions as a function of  $z$ . (b) FEM-simulated dispersion relations near the second stop band. Insets with blue and red colors illustrate the spatial electric field ( $E_y$ ) distributions of the band edge modes at the  $y = 0$  plane. Vertical dotted lines represent the mirror planes in the computational cells. (c) Calculated radiative  $Q$  factors of the upper and lower bands. (d) Evolution of transmission spectra vs the incident angle  $\theta$ . In the FEM simulations, we use the structural parameters  $\epsilon_{avg} = 4.00$ ,  $\Delta\epsilon = 1.00$ ,  $\epsilon_s = 1.00$ ,  $t = 0.50 \Lambda$ , and  $\rho = 0.40$ .

bands irrespective of lattice parameters such as  $t$ ,  $\Delta\epsilon$ , and  $\rho$ , they could find useful applications to overcome the discrete nature of the high- $Q$  resonant mode in conventional photonic lattices. As an example of the possible applications of the high- $Q$  bound states in the FCE metasurface, discussion on the Dirac cone dispersion is presented in the Supplemental Material [30].

We next show that the radiative  $Q$  factors in the 2D lattices can also be increased by eliminating the appropriate Fourier components in the original dielectric function. As illustrated in Fig. 3(a), we consider a simplest 2D lattice composed of square array of square-shaped high dielectric constant ( $\epsilon_a$ ) materials in the background medium with low dielectric constant ( $\epsilon_b$ ). The

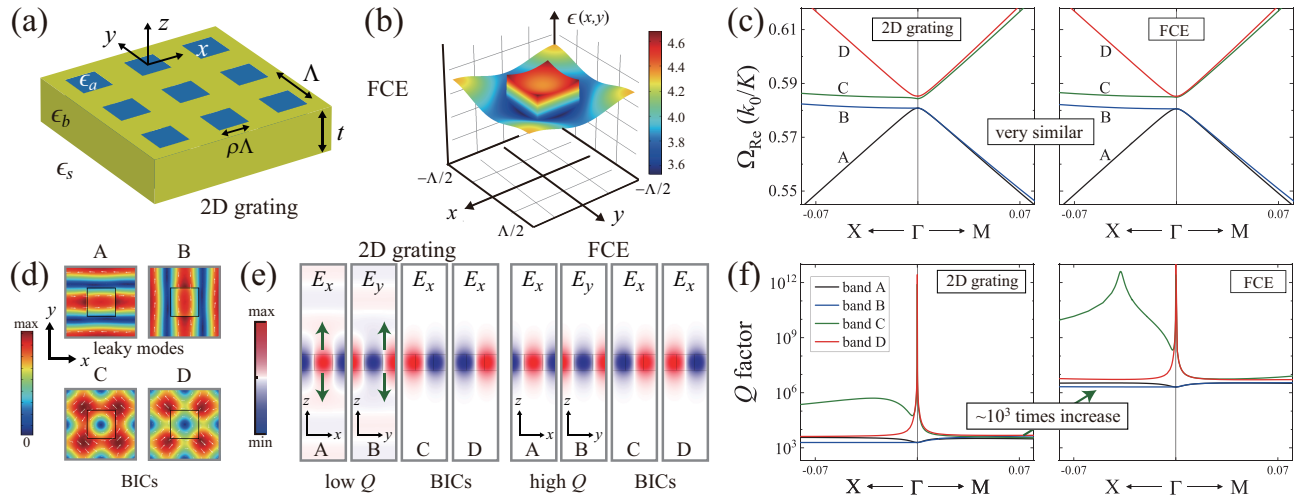


FIG. 3. (a) Schematic of a 2D grating. (b) Dielectric constant profile of the FCE metasurface corresponds to the 2D grating. (c) Simulated dispersion relations of the Bloch modes in the conventional 2D grating and FCE metasurface. (d) Simulated spatial electric field ( $|\mathbf{E}|$ ) distributions of the four band edge modes of the 2D grating at  $z = 0$  plane. White arrows represent in-plane electric field vectors. (e) Spatial electric field,  $E_x$  ( $E_y$ ), distributions of the band edge modes in the 2D grating and FCE metasurface at  $y = 0$  ( $x = 0$ ) plane. (f) Simulated radiative  $Q$  factors in the conventional 2D grating and FCE metasurface. In the simulations, we use the lattice parameters  $\Delta\epsilon = \epsilon_a - \epsilon_b = 1.00$ ,  $\rho = 0.40$ ,  $\epsilon_{avg} = 4.00$ ,  $t = 0.50 \Lambda$ , and  $\epsilon_s = 1.00$ .

average dielectric constant of the 2D lattice is given by  $\epsilon_{avg} = \rho^2\epsilon_a + (1 - \rho^2)\epsilon_b$ . For the 2D lattice shown in Fig. 3(a), the dielectric function can be expanded as

$$\epsilon(x, y) = \epsilon_{0,0} + \sum_{(m,n) \neq (0,0)}^{\infty} \gamma_{m,n} e^{i(mKx+nKy)}, \quad (6)$$

where the Fourier coefficients are given by  $\epsilon_{0,0} = \epsilon_{avg}$  and  $\gamma_{m,n} = \rho^2\Delta\epsilon \times \text{sinc}(m\pi\rho) \times \text{sinc}(n\pi\rho)$ .

In the 1D case, the first Fourier component with the spatial period of  $\Lambda$  was removed from the step-like original dielectric function. As the extension of the 1D study to the 2D grating structure, we remove the two Fourier harmonic components,  $2\gamma_{1,0} \cos(Kx)$  and  $2\gamma_{0,1} \cos(Ky)$  with the spatial period of  $\Lambda$ , from the original dielectric function, as illustrated in Fig. 3(b). Figure 3(c) shows that the second band gaps open at the  $\Gamma$  point, and the dispersion curves for the conventional 2D grating and FCE metasurface are very similar. There are four bands, A, B, C, and D, in the vicinity of the  $\Gamma$  point [32]. Figure 3(d) illustrates the simulated spatial electric field ( $|\mathbf{E}|$ ) distributions of the four band edge modes at  $z = 0$  plane. Band edge modes in A and B are degenerate and radiative out of the grating, but band edge modes in C and D are generally not degenerated and nonleaky because they are protected by the symmetry nature; field patterns in the FCE metasurface are not plotted because they are almost same as those for the conventional 2D grating. Radiative properties of the band edge modes can be clearly seen by investigating the spatial electric field  $E_x$  ( $E_y$ ) distributions at  $y = 0$  ( $x = 0$ ) plane. As shown in Fig. 3(e), asymmetric band edge modes in C and D are nonleaky BICs in both the conventional 2D grating

and FCE metasurface. However, symmetric band edge modes in A and B are radiative in the conventional 2D grating, while those are well confined in the FCE metasurface. The existence of the BICs can be seen from the radiative  $Q$  factors plotted in Fig. 3(f). In both the conventional 2D grating and FCE lattice, the symmetry-protected BICs in the band C and D exhibit  $Q$  factors larger than  $10^{12}$  at the  $\Gamma$  point but the  $Q$  values decrease noticeably as  $k_z$  away from the  $\Gamma$  point. However, simulated radiative  $Q$  factors in the FCE metasurface are approximately  $2 \times 10^3$  times larger than those in the conventional 2D grating.

In this study, we demonstrated that the radiative  $Q$  factors of Bloch modes in 1D and 2D photonic lattices can be increased noticeably by eliminating appropriate Fourier components in the spatially modulated dielectric function. Since the dielectric functions of the FCE metasurfaces shown in Fig. 2(a) and Fig. 3(b) have some fine details that require elaborate techniques, the practical implementation of the FCE metasurface with the engineered spatial dielectric function is challengeable. Currently, the required dielectric constant profile can be implemented in the long wavelength region, such as microwave, where diverse metamaterials consisting of deep subwavelength size components are feasible [33, 34]. As the nanofabrication technology continue to improve, it could be possible to realize the FCE metasurface operating at optical wavelengths in the future. To see this, as shown in Fig. 4(a), we consider a 1D silicon-air metasurface consisting of air slits,  $S_j$ , in a silicon slab ( $\epsilon_{Si} = 12.11$  at  $\lambda = 1.55 \mu m$ ). Based on the effective medium theory [35], twenty of air slits are appropriately located in the

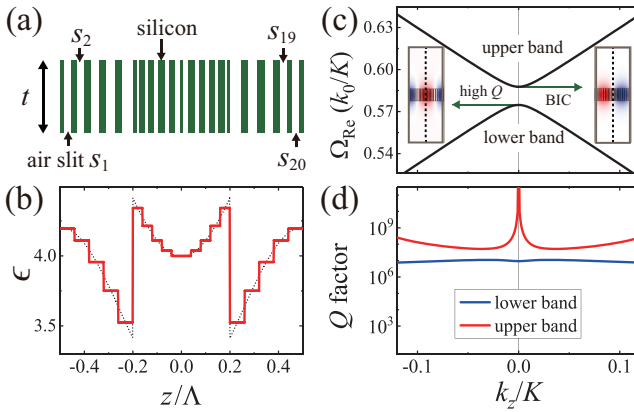


FIG. 4. (a) Schematic of a 1D silicon-air metasurface with  $t = 0.50 \text{ \AA}$ . (b) Effective dielectric constant of the silicon-air metasurface in the computational unit cell. Dotted line represents the dielectric constant of the FCE metasurface. FEM-simulated dispersion relations (c) and radiative  $Q$  factors (d) near the second stop band of the silicon-air metasurface.

unit cell of size  $\Lambda$  such that the effective dielectric function of the silicon-air metasurface mimics that of the FCE metasurface as illustrated in Fig. 4(b). Even though the effective dielectric function of the silicon-air metasurface varies in discrete steps, not only the dispersion curves of the silicon-air metasurface in Fig. 4(c) are nearly the same as those of the FCE metasurface in Fig. 2(b) but also the radiative  $Q$  factors in the silicon-air metasurface in Fig. 4(d) are comparable to the high- $Q$  values in the FCE-metasurface in Fig. 2(c). The radiative  $Q$  factors in the silicon-air metasurface are approximately  $10^4$  times larger than those in the conventional BDG in Fig. 2(c). From Fig. 4, it is reasonable to infer that the high- $Q$  values in the FCE metasurfaces are not affected seriously by the small imperfections introduced in the engineered dielectric constant profile.

We note that the proposed concept of eliminating Fourier harmonic components can be extended to the zero-contrast grating (ZCG) structures [36, 37]. Because the ZCG exhibits photonic band gaps and leaky-wave effects due to the spatially modulated thickness profile, the FCE metasurface corresponds to the ZCG can be designed by eliminating the first Fourier harmonic component in the spatially modulated thickness profile. We verified that the radiative  $Q$  factors in the FCE metasurface corresponds to the ZCG are noticeably increased due to the absence of the first Fourier harmonic component in the spatial thickness profile (see the Supplemental Material [30]). In a practical point of view, manipulation of the spatial thickness profile is more realistic than that of the spatial permittivity profile. Current state-of-the-art nanofabrication technology could be utilized to implement the required spatial thickness profile in the unit cell with the submicron size [38–40]. It is also presented in the Supplemental Material [30] that the radiative  $Q$

factors in the FCE metasurface are not affected seriously by the small imperfections introduced in the engineered thickness profile.

In conclusion, we introduced the concept of FCE metasurfaces that do not possess the first Fourier harmonic component in the spatially modulated lattice parameters, such as the dielectric constant and thickness, and demonstrated that the new types of lattices with 1D and 2D geometries support the continuous quasi-BICs in the vicinity of the second stop bands. The FCE metasurfaces exhibit noticeably increased radiative  $Q$  factors because the out-of-plane radiation is due to the first Fourier harmonic component of the periodic modulation in lattice parameters. Since the continuous high- $Q$  bound states are robust to the small imperfections introduced in the engineered thickness profile and dielectric function, the FCE metasurfaces can be utilized in various applications associated with high- $Q$  resonant Bloch modes.

This research was supported by grants from the National Research Foundation of Korea funded by the Ministry of Education (Nos. 2020R1I1A1A01073945 and 2018R1D1A1B07050116) and Ministry of Science and ICT (No. 2020R1F1A1050227), along with the Gwangju Institute of Science and Technology Research Institute in 2020.

\* sungooleee@gmail.com

† cskee@gist.ac.kr

- [1] A. V. Kildishev, A. Boltasseva, and V. M. Shalaev, *Science* **339**, 1232009 (2013).
- [2] N. Yu and F. Capasso, *Nat. Mater.* **13**, 139–150 (2014).
- [3] S. Sun, Q. He, J. Hao, S. Xiao, and L. Zhou, *Adv. Opt. Photonics* **11**, 38–479 (2019).
- [4] J. D. Joannopoulos, R. D. Meade, and J. N. Winn, *Photonic Crystals: Molding the Flow of Light*, (Princeton University, 1995).
- [5] G. Johnson, S. Fan, P. Villeneuve, J. D. Joannopoulos, and L. Kolodziejski, *Phys. Rev. B* **60**, 5751–5758 (1999).
- [6] M. Born and E. Wolf, *Principles of Optics*, (Cambridge University Press, Cambridge, 2002).
- [7] Y. H. Ko and R. Magnusson, *Optica* **5**, 289–294 (2018).
- [8] A. Arbabi, Y. Horie, M. Bagheri, and A. Faraon, *Nat. Nanotechnol.* **10**, 937–943 (2015).
- [9] A. M. H. Wong and G. V. Eleftheriades, *Phys. Rev. X* **8**(1), 011036 (2018).
- [10] M. Niraula, J. W. Yoon, and R. Magnusson, *Opt. Lett.* **40**, 5062–5065 (2015).
- [11] D. C. Marinica, A. G. Borisov, and S. V. Shabanov, *Phys. Rev. Lett.* **100**, 183902 (2008).
- [12] Y. Plotnik, O. Peleg, F. Dreisow, M. Heinrich, S. Nolte, A. Szameit, and M. Segev, *Phys. Rev. Lett.* **107**, 183901 (2011).
- [13] C. W. Hsu, B. Zhen, A. D. Stone, J. D. Joannopoulos, and M. Soljačić, *Nat. Rev. Mater.* **1**, 1–13 (2016).
- [14] K. Koshelev, G. Favraud, A. Bogdanov, Y. Kivshar, and A. Fratalocchi, *Nanophotonics* **8**, 725–745 (2019).
- [15] K. Koshelev, S. Lepeshov, M. Liu, A. Bogdanov, and Y.

Kivshar, Phys. Rev. Lett. **121**(19), 193903 (2018).

[16] K. Koshelev, S. Kruk, E. Melik-Gaykazyan, H.-H. Choi, A. Bogdanov, H.-G. Park, Y. Kivshar, Science **367**, 288–292 (2020).

[17] B. Zhen, C. W. Hsu, L. Lu, A. D. Stone, and M. Soljačić, Phys. Rev. Lett. **113**(25), 257401 (2014).

[18] H. M. Doeleman, F. Monticone, W. Hollander, A. Alù, and A. F. Koenderink, Nat. Photonics **12**, 397–401 (2018).

[19] S. I. Azzam, V. M. Shalaev, A. Boltasseva, and A. V. Kildishev, Phys. Rev. Lett. **121**(25), 253901 (2018).

[20] Y. Yang, C. Peng, Y. Liang, Z. Li, and S. Noda, Phys. Rev. Lett. **113**(3), 037401 (2014).

[21] J. Jin, X. Yin, L. Ni, M. Soljačić, B. Zhen, and C. Peng, Nature **574**, 501–504 (2019).

[22] X. Yin, J. Jin, M. Soljačić, C. Peng, and B. Zhen, Nature **580**, 467–471 (2020).

[23] R. Mermet-Lyaudoz, F. Dubois, N. Hoang, E. Drouard, L. Berguiga, C. Seassal, X. Letartre, P. Viktorovitch, and H. S. Nguyen, arXiv:1905.03868 (2019).

[24] Y. Ding and R. Magnusson, Opt. Express **15**(2), 680–694 (2007).

[25] A. Yariv and P. Yeh, *Optical Waves in Crystals* (Wiley, New York, 1984).

[26] K. Inoue and K. Ohtaka, *Photonic Crystals: Physics, Fabrication and Applications* (Springer-Verlag Berlin Heidelberg, 2004.).

[27] R. F. Kazarinov and C. H. Henry, IEEE J. Quant. Elec-  
tronics **21**, 144–150 (1985).

[28] S.-G. Lee and R. Magnusson, Phys. Rev. B **99**(4), 045304 (2019).

[29] D. Rosenblatt, A. Sharon, and A. A. Friesem, IEEE J. Quant. Electronics **33**, 2038–2059 (1997).

[30] See Supplemental Material for (1) Semi-analytical dispersion model and (2) FCE metasurfaces correspond to the zero-contrast gratings.

[31] K. Srinivasan and O. Painter, Opt. Express **10**, 670–684 (2002).

[32] C. Peng, Y. Liang, K. Sakai, S. Iwahashi, and S. Noda, Phys. Rev. B **86**(3), 035108 (2012).

[33] D. Schurig, J. Mock, B. Justice, S. Cummer, J. Pendry, A. Starr, and D. Smith, Science **314**, 977 (2006).

[34] H. F. Ma and T. J. Cui, Nat. Commun. **1**(3), 21 (2010).

[35] C. W. Haggans, L. Li, and R. K. Kostuk, J. Opt. Soc. Am. A **10**, 2217–2225 (1993).

[36] R. Magnusson, Opt. Lett. **39**, 4337 (2014).

[37] M. Shokoh-Saremi and R. Magnusson, Opt. Lett. **39**, 6958 (2014).

[38] I. Staude and J. Schilling, Nat. Photonics **11**, 274–284 (2017).

[39] W. T. Chen, A. Y. Zhu, V. Sanjeev, M. Khorasaninejad, Z. Shi, E. Lee, and F. Capasso, Nat. Nanotechnol. **13**, 220–226 (2018).

[40] A. Nda, L. Hsu, J. Ha, J.-H Park, C. Chang-Hasnain, and B. Kanté B, Nat. Commun. **11** 1 (2020).